






In situ nitriding of Fe₂VAl during laser surface remelting to manipulate microstructure and crystalline defects

Leonie Gomell ^{1,*}, Shao-Pu Tsai ^{1,†}, Moritz Roscher,¹ Ruben Bueno Villoro ¹, Peter Konijnenberg ^{1,‡}, Stefan Zaefferer,¹ Christina Scheu,¹ and Baptiste Gault ^{1,2}

¹Max-Planck-Institut für Eisenforschung (MPIE) GmbH, Max-Planck-Str. 1, 40237 Düsseldorf, Germany

²Department of Materials, Royal School of Mines, Imperial College London, Prince Consort Road, London SW7 2BP, United Kingdom



(Received 10 March 2022; accepted 3 August 2022; published 29 August 2022)

Tailoring the physical properties of complex materials for targeted applications requires optimizing the microstructure and crystalline defects that influence electrical and thermal transport and mechanical properties. Laser surface remelting can be used to modify the subsurface microstructure of bulk materials and hence manipulate their properties locally. Here, we introduce an approach to perform remelting in a reactive nitrogen atmosphere to form nitrides and induce segregation of nitrogen to structural defects. These defects arise from the fast solidification of the full-Heusler Fe₂VAl compound that is a promising thermoelectric material. Advanced scanning electron microscopy, including electron channeling contrast imaging and three-dimensional electron backscatter diffraction, is complemented by atom probe tomography to study the distribution of crystalline defects and their local chemical composition. We reveal a high density of dislocations, which are stable due to their character as geometrically necessary dislocations. At these dislocations and low-angle grain boundaries, we observe segregation of nitrogen and vanadium, which can be enhanced by repeated remelting in nitrogen atmosphere. We propose that this approach can be generalized to other additive manufacturing processes to promote local segregation and precipitation states, thereby manipulating physical properties.

DOI: [10.1103/PhysRevMaterials.6.085405](https://doi.org/10.1103/PhysRevMaterials.6.085405)

I. INTRODUCTION

The microstructure of materials impacts their properties. For example, mechanical properties can be manipulated by segregation to grain boundaries [1–4]. For functional materials, like thermoelectric materials, microstructural engineering was shown to be effective in modifying transport properties and thereby increasing the conversion performance [5–7]. A defect-rich microstructure can lead to a reduction in thermal conductivity [8–12], which increases the thermoelectric performance. To fully understand the impact of the microstructure, it needs to be investigated from near-atomic to millimeter length scales.

Additive manufacturing has been rising in prominence over the past decades to enable the fabrication of complex parts with near net-shape and in three dimensions (3D), for instance, through selective laser melting [13]. The thermal history of the build made by selective laser melting has been reported to generate complex microstructures [14–16]. Further, it offers opportunities for designing alloys and pro-

cesses to provide materials with unprecedented combinations of properties [17,18]. These benefits also have the potential to improve the performance of thermoelectric materials [19,20]. By adjusting the processing parameters, the microstructure, and hence properties, can be manipulated [21].

Of all the thermoelectric materials, we selected the promising full-Heusler Fe₂VAl compound. To gain insights into the as-built microstructures of selective laser melting processed Fe₂VAl, while avoiding the complexity the building process would create, we recently used laser surface remelting to manipulate the microstructure of casted Fe₂VAl locally [21]. Local measurements of the transport properties were correlated with advanced microstructural analysis to discuss the influence of structural defects [22]. Indeed, while some of these defects are easily visible using optical or scanning electron microscopy (SEM), others require near-atomic-scale analyses, which can be performed by atom probe tomography (APT). For Fe₂VAl, we showed vanadium nitride precipitates and/or segregation of V and N to dislocations, phase, and grain boundaries, which led to an increase in thermoelectric performance [22,23]. Vanadium nitrides act as phonon scattering centers, reducing the thermal conductivity, which in turn increases the figure of merit [22]. The nitrogen in these earlier studies was an impurity uncontrollably introduced during the processing of the bulk samples.

The route for microstructural manipulations by using *in situ* reactions during selective laser melting or laser surface remelting processing has been overlooked and will therefore be the focus of this paper. During the remelting process, the material interacts with the surrounding atmosphere. Oxygen pickup is a notorious issue that leads to unwanted oxidization

*Corresponding author: l.gomell@mpie.de

†Present address: National Taiwan University, Taipei City, Taiwan 10617.

‡Present address: Forschungszentrum Jülich, IAS-9, Germany.

Published by the American Physical Society under the terms of the [Creative Commons Attribution 4.0 International license](https://creativecommons.org/licenses/by/4.0/). Further distribution of this work must maintain attribution to the author(s) and the published article's title, journal citation, and DOI. Open access publication funded by the Max Planck Society.

or to O contents outside the specifications for safe usage of, e.g., Ti alloys [24,25]. Contrarily, *in situ* nitriding may help to increase the performance of the material, both in terms of thermoelectric and mechanical properties [26–29].

Here, we show that the nitrogen concentration at defects can be controlled by laser surface remelting. By changing the protective atmosphere in the processing chamber from Ar to N₂, we show that nitrogen can react with vanadium during remelting. Upon multiple passes, we find an increased nitrogen concentration in the sample. If the performance of a thermoelectric generator depends on the microstructure, the stability of the microstructure is also essential, even if it is often overlooked. We performed heat treatments *ex situ* at 500 K for up to 100 h and found that the dislocations and grain boundaries are stable due to their characteristic as geometrically necessary dislocations (GNDs). Microstructural manipulation by laser surface remelting or even extended to selective laser melting is not limited to Fe₂VAI but can be used to change the properties of other intermetallic compounds containing reactive metals in a reactive atmosphere in a similar manner.

II. EXPERIMENTAL METHODS

We synthesized Fe₂VAI by melting stoichiometric amounts of pure Fe (99.9%, Carboleg GmbH), Al (99.7%, Aluminium Norf GmbH), and V (99.9%, HMW Hauner GmbH) in an arc furnace. The sample was flipped over and remelted four times to ensure homogeneity. The average composition was obtained by inductively coupled plasma optical emission spectrometry to be Fe_{50.07}V_{24.93}Al_{25.95} (at. %). The casted sample was ground down to 600 grit SiC paper to ensure a homogeneous surface for laser surface remelting.

The ytterbium-fiber laser used has a wavelength of 1070 nm and is focused to a spot size of 90 μm. The laser scanning speed was 1400 mm/s, and the laser power was set to 200 W. The scanning strategy consists of single lines, which are separated by at least 0.5 mm. Between the remelting of the different lines, the sample was allowed to cool down to room temperature by pausing for 90 s. Some lines were remelted 3× and 5× on the same track. The remelting process was performed in an inert argon atmosphere or a reactive N₂ atmosphere to induce *in situ* nitriding. In the following, these samples will be called LSR_{Ar} and LSR_N, respectively. The residual oxygen concentration was <80 ppm.

Microstructural investigations using SEM, including electron backscattered diffraction (EBSD), energy-dispersive x-ray spectroscopy (EDX), and electron channeling contrast imaging (ECCI) were performed in cross-sectional and top views. Before the microscopy experiments, the samples were polished down to 0.05 μm colloidal silica. In the top view, these samples were imaged without polishing and after grinding of ~5 and 20 μm, like the samples remelted in Ar atmosphere presented in Ref. [22]. These samples will be called top₀, top₅, and top₂₀ in the following. The top₅ sample is also used for investigations of the stability of defects. The samples were held at 500 K for 2 h before a second investigation and additionally for 5 d before a third investigation of the microstructure. The temperature was chosen in agreement with the peak *zT* temperature of thermoelectric Fe₂VAI [30,31]. To avoid oxidation during the annealing process, the

annealing chamber was flooded with Ar gas, and a Ta getter was used.

For SEM imaging in backscattered electron (BSE) mode and ECCI, a Zeiss SEM 450 was used. EBSD and EDX were performed in a Zeiss Sigma, equipped with an EDAX OIM EBSD System with a Hikari camera. The acceleration voltage was set to 15 kV for EDX, 20 kV for EBSD, and 30 kV for ECCI. ECCI was used for direct observation of dislocations and other defects and for calculating the dislocation density. Two-dimensional (2D) EBSD mapping was conducted with a step size of 200 nm on a hexagonal grid. Furthermore, large-volume 3D EBSD was performed using the in-house built automated system ELAVO 3D [32], which is based on automated serial polishing combined with automated EBSD mapping. Controlled polishing is performed with a QATM Saphir X-Change autopolishing machine. On the present material, a removal rate of ~1 μm was achieved by polishing with 1 μm diamond suspension for 80 s, 50 nm oxide suspension polishing for 360 s, and sufficient cleaning. The removal rate was determined by an M-shaped pattern applied to a sample side perpendicular to the surface of interest using an FEI Helios plasma focused-ion beam (FIB). The used parameters are summarized in Table S1, and the removal rate is displayed in Fig. S1 in the Supplemental Material [36]. A Universal Robots UR5 transfers the sample between a Zeiss Crossbeam 1540 XB SEM and the polishing station. For 3D EBSD, a cubic measurement raster with a voxel size of 1 μm³ was chosen. Each volume contains 100 slices, translating into a measured depth of 100 μm. Due to the different sizes of the melt pools, the analyzed volume varies between ~700 000 and 1 900 000 μm³ for the 1× and 5× remelted samples, respectively. An in-house version (2.0.22.2000) of the QUBE software package was used for postprocessing of all 3D datasets [33].

Near atomic-scale investigations were performed by APT. A dual-beam FIB instrument (FEI Helios Nanolab 600/600i), equipped with a Ga⁺ ion source, was used to prepare needle-shaped specimens. The lift-out was prepared from the cross-section at a position ~5 μm below the surface. The procedure is described in Ref. [34]. APT was conducted using a LEAP 5000 XS instrument (Cameca Instruments) operated in laser pulsing mode. The pulse energy was set to 50 pJ, the pulse repetition rate to 200 kHz, and the detection rate to 2%. The base temperature was kept at 60 K. The data were reconstructed and analyzed by AP Suite 6.1 (Cameca Instruments).

III. RESULTS AND DISCUSSION

Figure 1 shows BSE images of the cross-section of 1×, 3×, and 5× remelted melt pools of the LSR_{Ar} and LSR_N samples [Figs. 1(a) and 1(b), respectively]. The position in relation to the melt pool is sketched next to the images. BSE images in the top view are displayed in Fig. S2 in the Supplemental Material [36]. The atmosphere does not influence the microstructure on a scale noticeable by BSE, EBSD, and EDX (Figs. 1, 2, S3, S7, and S8 in the Supplemental Material [36]). Hence, the higher thermal conductivity of N₂ compared with Ar [35], which was shown to change melt pool dimensions [29], can be neglected here. The thermal conductivity of the material is three orders of

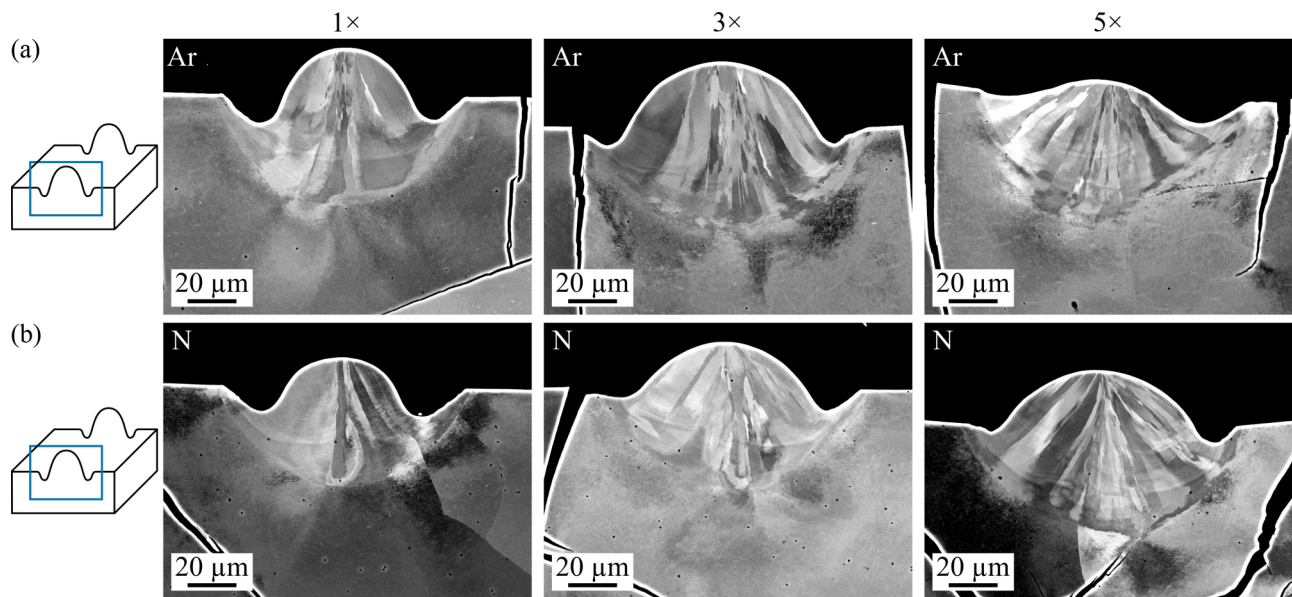


FIG. 1. Backscattered electron (BSE) images of the melt pool cross-section of (a) the LSR_{Ar} sample, (b) the LSR_N sample. The left, middle, and right columns show 1×, 3×, and 5× remelted regions. Small, elongated grains are observed in all melt pools.

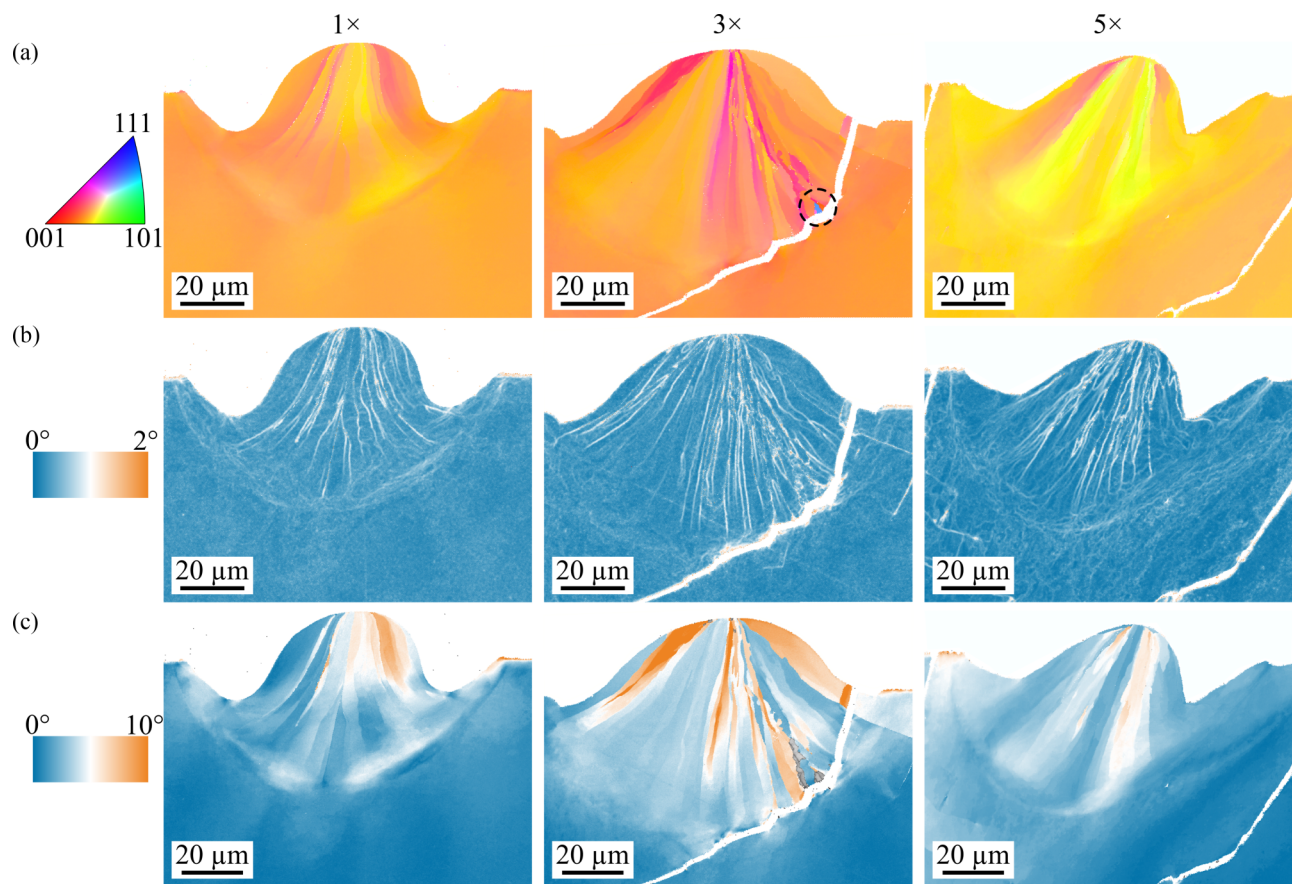


FIG. 2. Two-dimensional (2D) electron backscattered diffraction (EBSD) maps of the LSR_{Ar} sample after 1×, 3×, and 5× remelting. (a) Inverse pole figure (IPF) maps along sample normal direction, which is parallel to the laser scanning direction. Similar color coding reveals the strong texture and epitaxial growth. (b) Kernel average misorientation (KAM) maps, showing the misorientation between second nearest neighbors on a scale from 0° to 2°. The low-angle grain boundaries are clearly observed as white lines. (c) Grain reference orientation deviation (GROD) maps, showing the misorientation in relation to the substrate grain on a scale from 0° to 10°.

magnitude higher than that of the surrounding gases. Hence, the heat transport and solidification processes are guided by the properties of the material, and the influence of the gases are neglectable. This enables the use of the same processing parameters (i.e., laser scanning speed and laser power) without the need to optimize the parameters again after changing the atmosphere. Optimizing the processing parameters (for example, to reduce cracking or to adjust the melt pool size and grain size) is often a time-consuming task. Hence, changing the properties of a material by changing the atmosphere can be more easily applied than by changing the other process parameters.

All micrographs show elongated solidification cells, i.e., individual grains, which grow in a columnar fashion (Figs. 1 and S2 in the Supplemental Material [36]) from the substrate along the maximum thermal gradient directions. For all remelting conditions, cracks are observed, which appear at or close to high-angle grain boundaries of the underlying casted sample. The melt pool and grain sizes are given in Table S2 and discussed in the Supplemental Material [36]. In short, while the melt pool size increases for repeated remelting, the grain size decreases. Further, the melt pool is destabilized and exhibits fluctuations in size and shape after repeated remelting. While all $1\times$ remelted regions look similar, there are strong fluctuations for $3\times$ and $5\times$ remelted regions. This is the main reason for the increased standard deviations of the melt pool sizes, which are summarized in Table S2 in the Supplemental Material [36]. The 3D EBSD reconstructions (Fig. 3), which include $100\ \mu\text{m}$ of each molten track, similarly show a strongly fluctuating melt pool size for the $5\times$ remelted melt pool. This indicates that multiple remelting facilitates melt pool instabilities, which offers possibilities for even more complex microstructures than $1\times$ remelting.

Figures 2 and 3 show the 2D and 3D EBSD evaluations of the LSR_{Ar} sample, respectively. The 2D EBSD map is taken after finishing the 3D procedure at the last slice with a higher resolution. This enables us to analyze the grain structure and misorientations across grain boundaries in more detail. EBSD maps from the LSR_{N} samples in cross-sectional and top views are given in the Supplemental Material (Figs. S3 and S4) [36]. Figures 2(a), 3(a), and 3(b) show the inverse pole figure (IPF) map along laser scanning direction. For the 3D scan, different viewing directions are shown. In the melt pool region, newly solidified grains adopt almost the same orientation as the substrate, which indicates an epitaxial growth mechanism. This can be confirmed by almost the same color coding (orange). However, slight color contrast is observed in both the heat-affected zones and melt pool interiors, which is possibly due to strains caused by solidification. Within the $1\times$ remelted melt pool, a grain boundary of the casted grain is observed, indicated by the color contrast in the IPF. Its shape within the melt pool is discussed in more detail in the Supplemental Material (Fig. S5) [36].

No newly formed high-angle grain boundaries are observed in the melt pool, also not for repeatedly remelted regions, except for grains close to a crack in the $3\times$ remelted region. Here, 18 grains with a misorientation $> 5^\circ$ in relation to the substrate grain are found. These grains are shown in Supplemental Material Fig. S6 [36]. One of these grains is

also easily visible in Figs. 2(a), 3(a), and 3(b) (highlighted by the dashed circle), as it appears blue in the IPF map, indicating a normal close to (111) in the sample z direction. We attribute this growth behavior to the missing substrate grain for epitaxial growth. The crack was formed before the last remelting, and the melt was not able to close the crack before solidifying. Hence, instead of epitaxial growth, new grains nucleated with a random orientation. These grains then grew in the direction of the thermal gradient until they reached the surface.

The boundaries within the melt pool can be characterized by their misorientation. For 3D EBSD, Fig. 3(c) shows the local average disorientation (LAD). In 2D, a kernel average misorientation (KAM) map [Fig. 2(b)] and a grain reference orientation deviation (GROD) map [Fig. 2(c)] are used for visualization. The LAD and KAM maps show the average misorientation in relation to the next nearest neighbor in the kernel, while the GROD map indicates the misorientation of each point in relation to the mean grain orientation of the substrate as reference. Most boundaries show a misorientation angle of 1° – 2° . Compared with the substrate grain, the maximum misorientation is $\sim 10^\circ$. No clear trend of the misorientation could be observed for the multiple remelted regions. Due to the misorientations within the grains, dislocations are created to compensate for the strains generated. The KAM data are also used to calculate the density of the GNDs [37], as described in the Supplemental Material [36]. On average, a GND density of $1.2 \times 10^{13}\ \text{m}^{-2}$ is observed. To explain the formation of GNDs inside grains in melt pools, GROD axis analyses were carried out. However, the crystal rotations do not follow any clear or systematic trend. Further analyses must be conducted to understand the origin of crystal rotations inside each grain fully. In addition to this, the 3D EBSD data show that there is no significant evolution of microstructure along the scan track, i.e., most of the data can be well-interpreted by looking on 2D cross-sections.

A. SEM—ECCI

When the unpolished sample surface is analyzed more closely using ECCI, nanoplatelets are observed in the surface layer, which exclusively grow in N_2 but not in Ar atmosphere. Figure 4(a) shows the surface of the $\text{LSR}_{\text{Ar},1\times}$ sample. Dislocations with a density of $\sim 1 \times 10^{14}\ \text{m}^{-2}$ are observed as brightly imaged line features. The dislocations are aligned in a preferred direction, approximately parallel to the laser scanning direction. On the other hand, the surface of the LSR_{N} sample [Fig. 4(b)] does not show any dislocations but platelet-shaped precipitates, with an average length of $49 \pm 14\ \text{nm}$, an average width of a few nanometers, and a number density of $\sim 3 \times 10^{14}\ \text{m}^{-2}$. Similar precipitates can be found in the $3\times$ and $5\times$ remelted melt pools (Fig. S9 in the Supplemental Material [36]). Since these precipitates only grow in N_2 atmosphere and considering the previously observed tendency of V to form VN_x [23,38,39], we may assume that these precipitates are VN_x . Controlled ECCI (i.e., ECCI under well-controlled Bragg diffraction) was conducted on the $5\times$ remelted melt pool (inset in Fig. S9 in the Supplemental Material [36]), indicating that the precipitates lie on the (001) lattice plane of the host matrix, which is con-

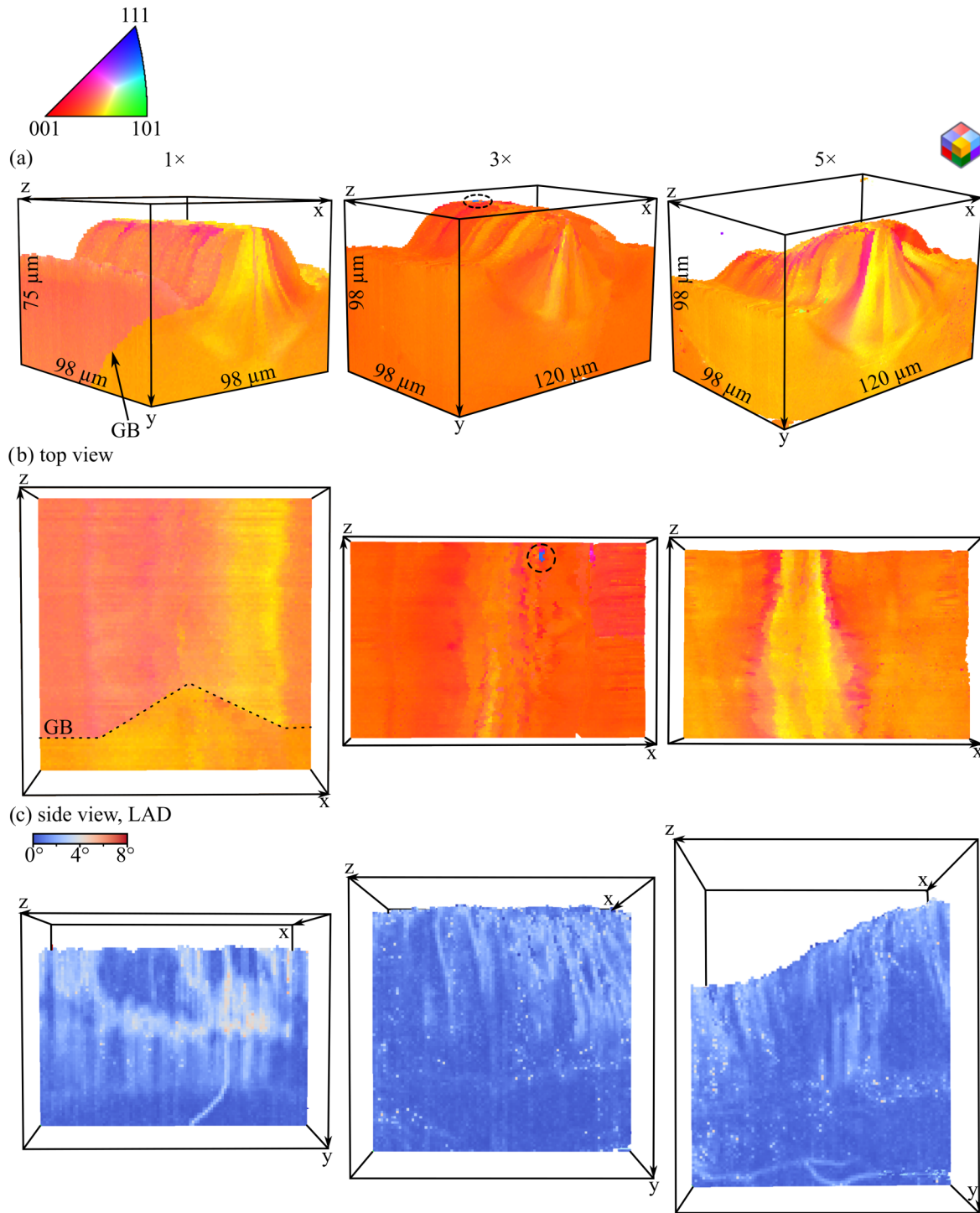


FIG. 3. Large-volume three-dimensional (3D) electron backscattered diffraction (EBSD) of the 1×, 3×, and 5× remelted tracks of the LSR_{Ar} sample. (a) and (b) Inverse pole figure (IPF), shown in different viewing directions. Slight color contrast reveals the texture and epitaxial growth within the melt pool. The dashed line marks the grain boundary of the substrate, and the dashed circle marks the non-epitaxially grown grain. (c) Local average disorientation (LAD) plot in side view, showing the low-angle grain boundaries in the melt pools.

sistent with the 90° angle found between individual particles visible in Fig. 4(b).

The precipitates only appear in a surface layer of the melt pool, which stays longer in contact with the N₂ atmosphere than the interior of the melt pool and is the last part to solidify. During solidification, most of the impurities remain in the melt and are expelled from the solid, like the typi-

cal Scheil model for solidification. The low solubility of N in Fe₂VAI was observed by APT previously [22,23,39] and will be shown again below: nitrogen segregates to dislocations and grain boundaries and is hardly found in the matrix (<0.1 at. %). The remaining melt enriches in N and gets increasingly supersaturated, facilitating the formation of precipitates in the steps of solidification. Additional reactions

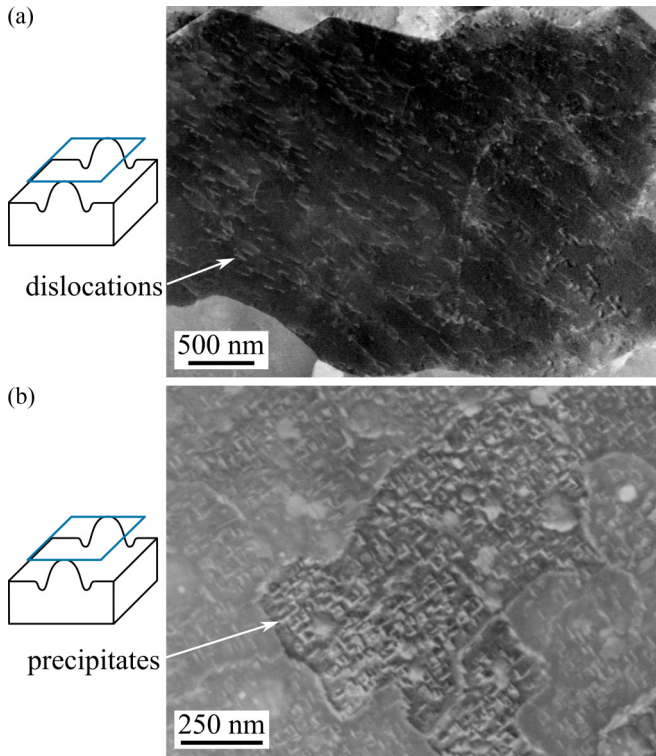


FIG. 4. Electron channeling contrast (ECC) images of the unpolished top_0 sample (a) $LSR_{Ar,1\times}$ and (b) $LSR_{N,1\times}$. The LSR_{Ar} sample shows brightly imaged dislocations, while the LSR_N sample shows platelet-shaped nanoprecipitates.

of the N_2 atmosphere and the solid at elevated temperatures might lead to further integration of N in the material.

If the top part is polished away and the top_5 sample is observed, only dislocations but no precipitates can be found in both the LSR_{Ar} and LSR_N samples (Fig. 5). The dislocation density is on the order of $3 \times 10^{13} m^{-2}$, which is slightly lower than that on the unpolished surface remelted in Ar atmosphere. No significant difference in dislocation density occurs between LSR_{Ar} and LSR_N samples or for the multiple times remelted regions. This density agrees well with the calculated GND density of $1 \times 10^{13} m^{-2}$, and hence, the dislocations found in ECCI can be classified as GNDs (i.e., they all have similar Burgers vectors).

GNDs are essential to accommodate the lattice rotations and can only annihilate by recrystallization at high temperatures. This is an advantage over other dislocations, which could migrate and annihilate at the working temperatures of a thermoelectric device, i.e., at 500 K for Fe_2VAl . To show that the dislocations found in the melt pool are stable, the same position is imaged before and after heat treatment for 2 h and additionally 5 d. Figure 5 shows the LSR_{Ar} and LSR_N samples remelted once. The $3\times$ and $5\times$ remelted samples are shown in the Supplemental Material (Fig. S10) [36]. By comparing the position and density of the dislocations and grain boundaries, we show evidence that they are stable. However, this experimental design has some drawbacks. Mirror forces might pin the observed dislocations to the surface, and dislocations within the bulk could behave differently and migrate. However, due to their character as GNDs, we can confidently claim that the microstructure generated by laser surface remelting is stable at the temperature of highest thermoelectric performance of Fe_2VAl . To finalize the ECCI investigations, Fig. S11 in the Supplemental Material [36] shows micrographs of grain boundaries. Single dislocations can be seen, confirming the low-angle grain boundary character observed by EBSD. The distance between the dislocations can be

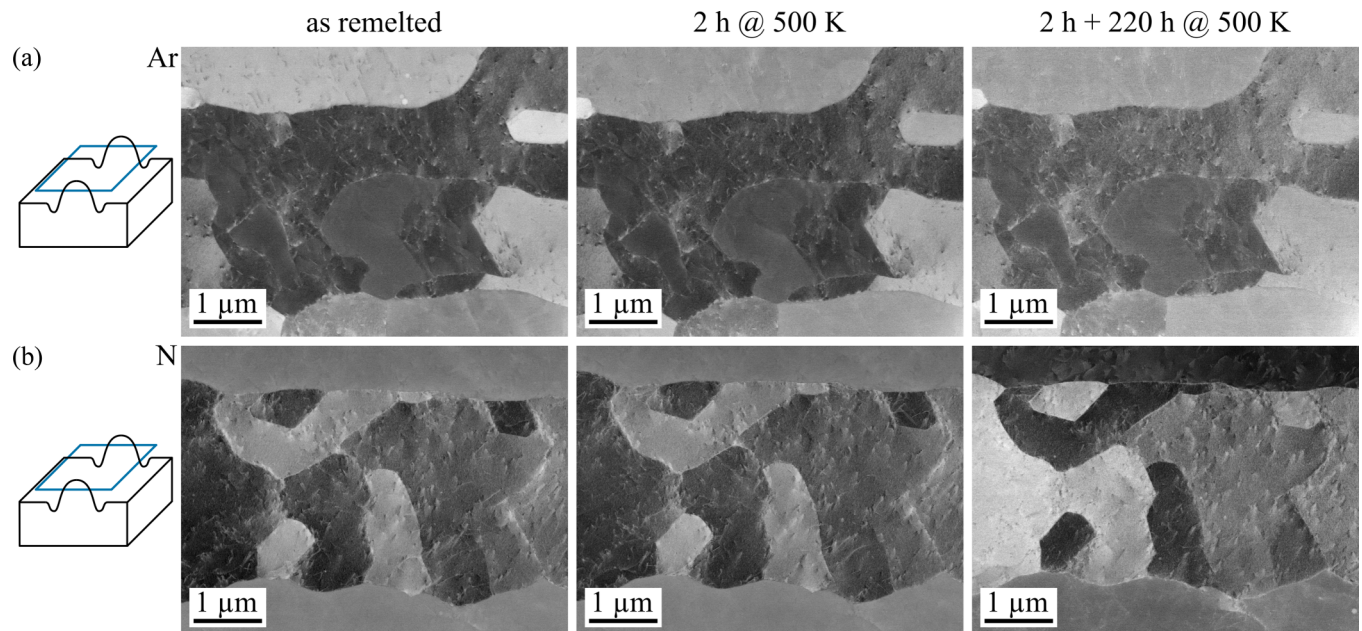


FIG. 5. Electron channeling contrast (ECC) images of the top_5 sample (a) $LSR_{Ar,1\times}$ and (b) $LSR_{N,1\times}$. The positions of the grain boundaries and dislocations do not change after heat treatment, indicating a stable microstructure. Contrast variations in the images are due to different channeling conditions.

TABLE I. Averaged composition of the different specimens determined by APT. For every sample, > 200 million ions have been measured. The composition of the substrate, determined by ICP-OES, is given for comparison.

Sample	Fe (at. %)	V (at. %)	Al (at. %)	N (at. %)
1×, Ar	49.9 ± 0.1	26.3 ± 0.1	23.8 ± 0.1	0.02 ± 0.02
3×, Ar	50.2 ± 0.1	27.2 ± 0.1	22.6 ± 0.1	0.02 ± 0.02
5×, Ar	50.4 ± 0.1	28.1 ± 0.1	21.4 ± 0.1	0.03 ± 0.02
1×, N	50.0 ± 0.1	26.2 ± 0.1	23.9 ± 0.1	0.02 ± 0.02
3×, N	50.4 ± 0.1	26.8 ± 0.1	22.7 ± 0.1	0.04 ± 0.03
5×, N	50.2 ± 0.1	27.8 ± 0.1	22.0 ± 0.1	0.08 ± 0.03
Substrate (ICP-OES)	50.07	24.93	25.95	0.01

used to calculate the misorientation angle (Supplemental Material [36]).

B. APT—nanoscale compositional analysis

Using SEM methods, no indication of nitriding was observed within the melt pool interior, only on the surface. APT is then used to quantify the composition on the nanometer scale. The APT specimens were taken ~5 μm below the surface, and hence, the precipitates shown in Fig. 4 were not observed. Here, 1×, 3×, and 5× remelted melt pools of the LSR_{Ar} and LSR_N samples are compared.

In a first step, the composition of the APT specimens is analyzed and given in Table I. A constant and small amount of N is found in the LSR_{Ar} sample, which can be attributed to impurities of the raw material and to residual N₂ in the atmosphere during casting. The LSR_{N,1×} sample shows no increase in overall N concentration, but the N content is increased after repeated remelting. All nitrogen is detected as VN⁺ or VN²⁺ molecular ions typically detected in (carbo)nitride precipitates in Fe-based materials [40,41] and decomposed to obtain the N composition. Remelting further changes the composition: Al is preferentially lost during this process, as observed by APT analyses and EDX maps (Figs. S7 and S8 in the Supplemental Material [36]). This loss is attributed to preferential spatter and evaporation of Al [22]. While Al is depleted, the V composition is increased slightly. Such an off-stoichiometric composition of Fe₂V_{1-x}Al_{1+x} ($x < 0$) was shown to increase the thermoelectric figure of merit up to 0.13 due to an optimized charge carrier concentration [30,42].

In a second step, the composition of clusters, dislocations, and low-angle grain boundaries is analyzed. These defects are known to introduce phonon scattering centers, which decrease the thermal conductivity and hence increase the thermoelectric performance [43–46]. VN_x clusters, indicated by an isocomposition surface of 1 at.% N (Fig. 6), are only found in the sample remelted 3× and 5× in nitrogen atmosphere. As random fluctuations in the dataset can also create very small clusters, only clusters >3 nm³ are considered in the calculations. Figure 6 shows the cluster composition, calculated as a proxigram, and the nearest neighbor distribution, indicating the nonrandom clustering of VN molecular ions. The proxigram shows the enrichment of V and N together with a depletion of Fe and Al. For both the 3× and 5× remelted specimens, the maximum N concentration is ~8 at.%, an increase of two orders of magnitude compared with the average N concentration. The composition of

the clusters was determined using 1D-compositional profiles of five individual clusters (not shown) to be Fe_{27±5}V_{53±7}Al_{12±3}N_{8±1} (at.%). The impact of nanoparticles on the thermoelectric properties, especially the thermal conductivity, was discussed by Mingo *et al.* [43] on the example of silicide nanoparticles in SiGe. They showed a reduction in thermal conductivity due to phonon scattering at the nanoparticles. Hence, we anticipate that the clusters observed in the LSR_N specimens will also contribute to a reduction of the thermal conductivity.

Dislocations, including GNDs, within the melt pool can scatter phonons by their strain field and core. In Ref. [22], we reported a decrease of the thermal conductivity after 1× remelting in Ar atmosphere, attributed to dislocation

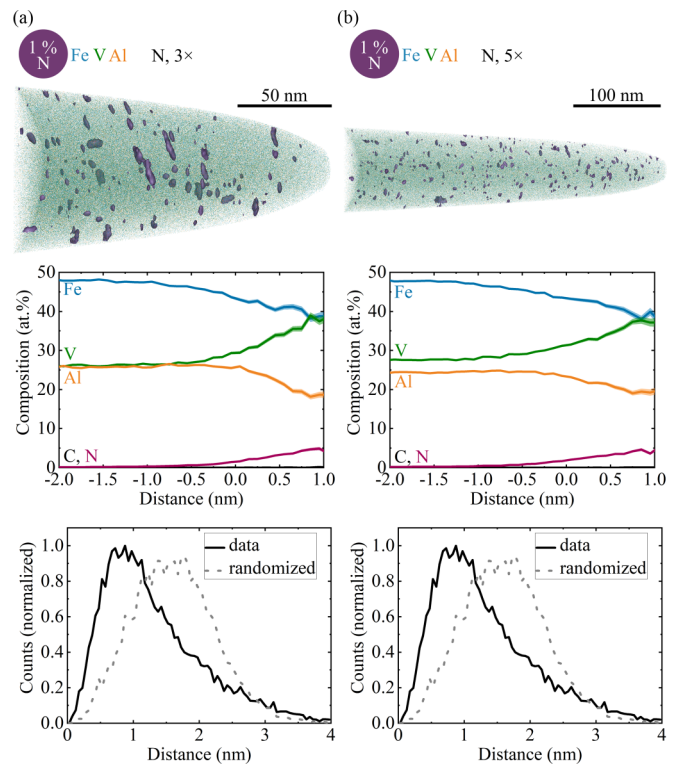


FIG. 6. Atom probe tomography (APT) reconstruction of LSR_N specimens after (a) 3× and (b) 5× remelting. Clusters are found in both specimens, while they could not be observed in the other specimens. The proxigram shows the composition of the clusters, which are enriched in V and N and depleted in Fe and Al. The cluster count distribution plotted for VN molecular ions suggests significant clustering.

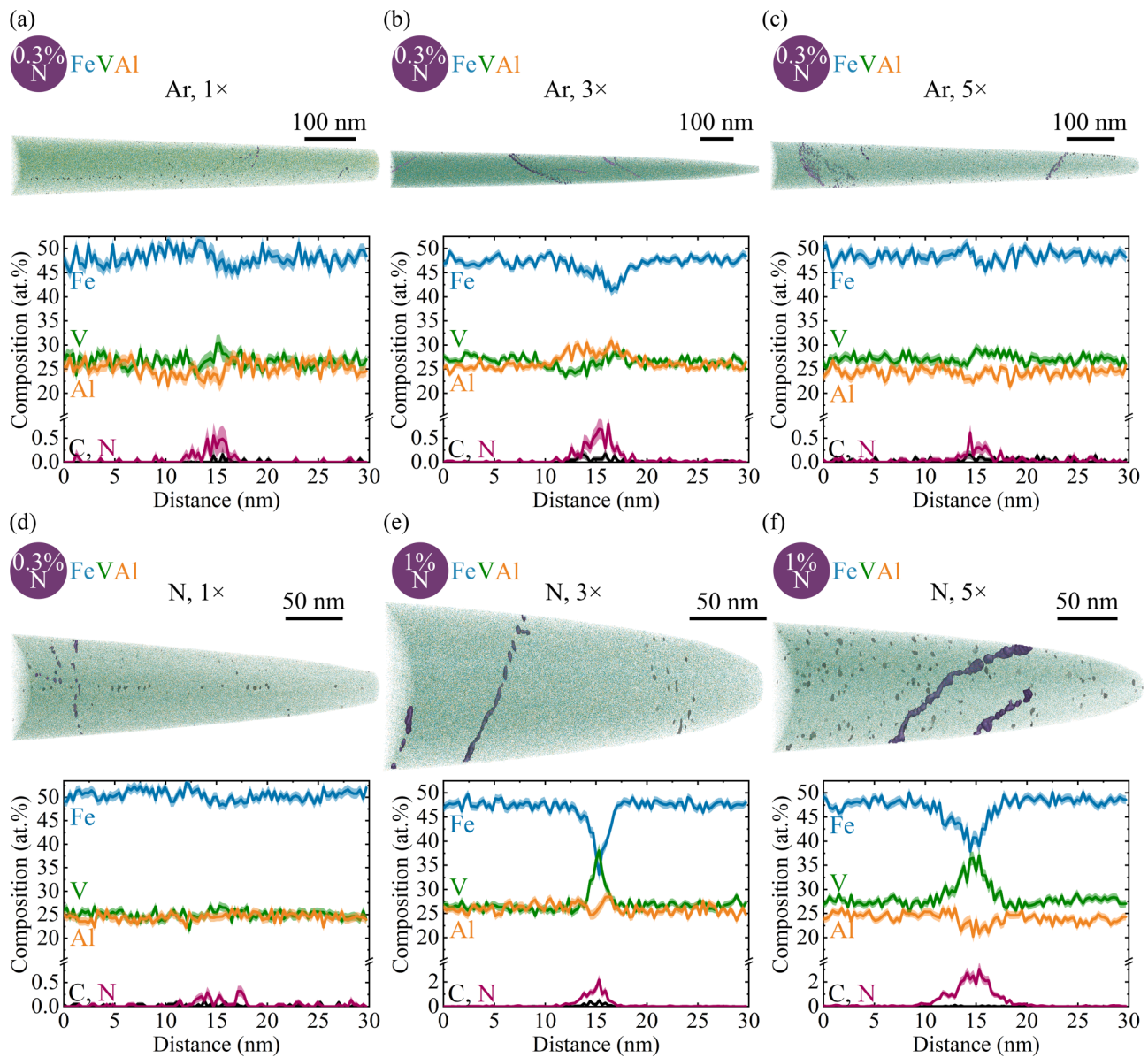


FIG. 7. Atom probe tomography (APT) reconstruction of specimens, selected to analyze dislocations, observed due to segregation. The segregation is visualized by isocomposition surfaces with a threshold given in the figure. The compositional profiles are calculated using a cuboidal region of interest with a size of $30 \times 5 \times 30 \text{ nm}^3$. (a) $\text{LSR}_{\text{Ar},1\times}$, (b) $\text{LSR}_{\text{Ar},3\times}$, (c) $\text{LSR}_{\text{Ar},5\times}$, (d) $\text{SN}_{\text{N},1\times}$, (e) $\text{LSR}_{\text{N},3\times}$, and (f) $\text{LSR}_{\text{N},5\times}$.

scattering. As core scattering depends on the presence of a Cottrell atmosphere [45,46], we assume that a change in the composition due to nitriding will further affect the thermal transport. The Cottrell atmosphere is observed by APT. Dislocations have been found by APT in all samples, as shown in Fig. 7. However, in the $\text{LSR}_{\text{N},3\times}$ and $\text{LSR}_{\text{N},5\times}$ samples, dislocations are easier to observe and visualize due to more pronounced segregation. Isocomposition surfaces of N are superimposed on the reconstructions, with the used concentration threshold given next to the reconstructions in Fig. 7. Randomly distributed clusters of isocomposition surfaces, not belonging to dislocations, are shown in transparent gray for better visualization of the features of interest. The LSR_{Ar} samples show little segregation of N toward the dislocations with a maximum concentration of $\sim 0.5 \text{ at.}\%$. It appears, like the cluster formation but with a less strong level, that nitrogen

is cosegregated by vanadium. Again, a depletion of Fe and Al is observed. The segregation of V and N can be increased by changing the atmosphere to N_2 . The maximum N concentrations at dislocations are ~ 0.5 , 2, and 2.5 at. % for the $1\times$, $3\times$, and $5\times$ remelted regions, respectively. Therefore, segregation could be increased by an order of magnitude compared with the LSR_{Ar} sample. In addition, also the V segregation and the depletion of Fe and Al are more pronounced. We attribute this to cosegregation of V and N, triggered by the higher N concentration.

In addition to individual dislocations within the grains, we observed segregation to dislocation arrays that constitute low-angle grain boundaries. Figure 8 shows APT reconstructions of the specimen with low-angle grain boundaries with the same isoconcentration surfaces as in Fig. 7. Mainly tilt boundaries with parallel dislocations are observed, but a twist

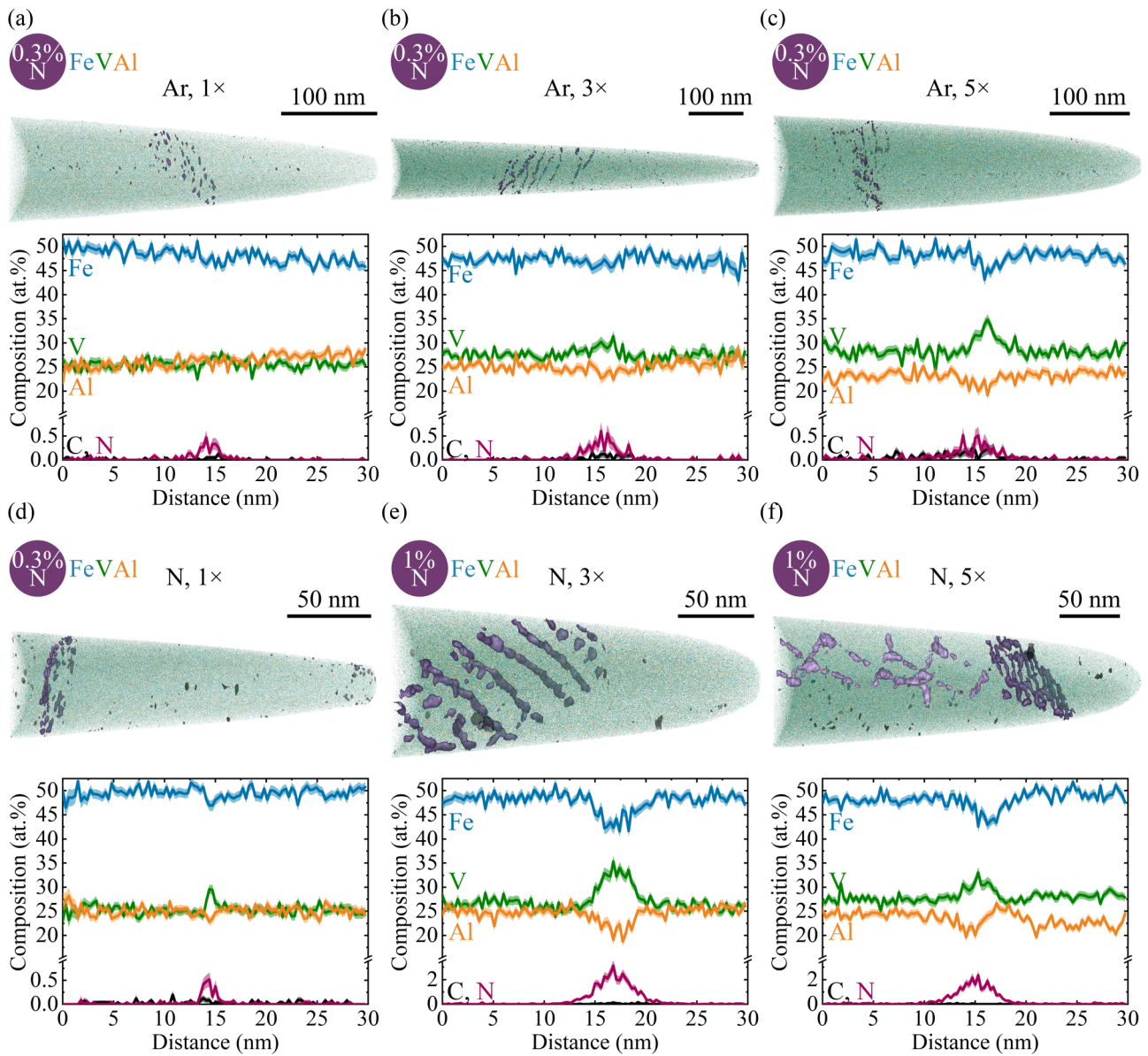


FIG. 8. Atom probe tomography (APT) reconstruction of specimens, selected to analyze grain boundaries, observed due to segregation. The segregation is visualized by isocomposition surfaces with a threshold given in the figure. The compositional profiles are calculated within an individual dislocation using a cuboidal region of interest with a size of $30 \times 5 \times 30 \text{ nm}^3$. (a) $\text{LSR}_{\text{Ar},1\times}$, (b) $\text{LSR}_{\text{Ar},3\times}$, (c) $\text{LSR}_{\text{Ar},5\times}$, (d) $\text{LSR}_{\text{N},1\times}$, (e) $\text{LSR}_{\text{N},3\times}$, and (f) $\text{LSR}_{\text{N},5\times}$.

boundary with crossed dislocation lines was found in the $\text{LSR}_{\text{N},5\times}$ sample. For tilt boundaries, the distance between the dislocations can be used to calculate the misorientation angle (see Supplemental Material [36]). Dislocation distances between 8 and 26.5 nm are found, translating into misorientations of 1.9° and 0.6° , which fit the EBSD results and confirm that these features are indeed dislocations.

Here, 1D concentration profiles in Figs. 7 and 8 reveal similar trends regardless of whether dislocations are individual ones or within low-angle grain boundaries. In addition, the level of segregation found at the dislocations which build up the low-angle grain boundaries is independent of the grain boundary misorientation angle. Hence, the averaged composition of the low-angle grain boundaries depends strongly on misorientation as the dislocation density increases with

misorientation angle. A twist boundary, visible in the $\text{LSR}_{\text{N},5\times}$ sample, shows crossed dislocations. At the crossing points, the N composition is increased up to 6 at. %. We assume that these positions are possible nucleation sites for precipitation.

Finally, the average nitrogen content of the defects in the different samples is compared. The maximum N composition was determined using the 1D compositional profile being fit to a Gaussian curve. The maximum value was obtained by averaging over 3 to 8 dislocations and 2 to 3 grain boundaries, with 3 to 4 dislocations taken in each boundary for every sample. The overall results are summarized in Fig. 9. As explained before, nitrogen segregation was found in all samples. However, while the composition stays roughly constant for the LSR_{Ar} sample, the N composition found in the LSR_{N} sample is strongly increased by repeated remelting. For $1\times$ remelting,

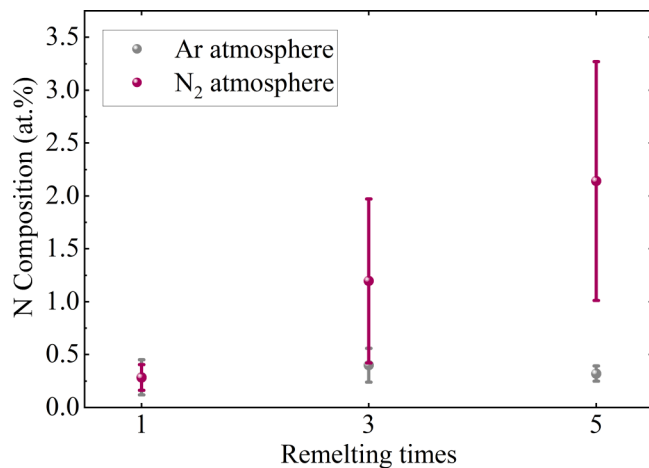


FIG. 9. Comparison of the N composition observed at dislocations and grain boundaries for LSR_{Ar} (gray) and LSR_N (dark red) samples. The error bars show the standard deviation of the calculation.

the composition of defects in the LSR_N sample is like that of the LSR_{Ar} samples. For the LSR_{N,1×} sample, the influence of nitrogen can only be observed at the surface in the form of nanoprecipitation, as indicated by ECCI measurements. Upon repeated remelting, these precipitates get turbulently mixed into the melt pool. During and after solidification, the inserted nitrogen cosegregates together with vanadium to dislocations and grain boundaries. For the 3× and 5× remelted regions, the N composition is increased by a factor of 4 or 8, respectively. As the interaction time between the atmosphere and the material cannot only be increased by repeated remelting but also by a reduction of the laser scanning speed, our approach of *in situ* nitriding offers the possibility to control the nitrogen composition at defects.

IV. CONCLUSIONS

To summarize, we present an approach to perform laser surface remelting in a reactive N₂ atmosphere to form nitrides and induce segregation of nitrogen to crystal defects on the example of thermoelectric full-Heusler compound Fe₂VAl. We show that the amount of nitrogen at dislocations and low-angle grain boundaries can be controlled by repeated remelting. An increase of nitrogen content by two orders of magnitude was revealed by APT. Nitrogen is cosegregated by vanadium, creating a VN_x Cottrell atmosphere around dislocations. Due to the strains within the melt pool area, a high density of GNDs on the order of 10¹³ m⁻² is observed by EBSD and visualized by ECCI. Our approach of *in situ* nitriding during remelting can be applied to other additive manufacturing processes, manipulating physical properties by inducing local segregation and precipitation.

ACKNOWLEDGMENTS

We thank U. Tezins, A. Sturm, M. Nellesen, C. Broß, and K. Angenendt for their technical support at the FIB/APT/SEM facilities at MPIE. LG gratefully acknowledges Studienstiftung des deutschen Volkes for funding. SPT acknowledges Nippon Steel Corporation for financial support. RBV acknowledges the International Max Planck Research School for Interface Controlled Materials for Energy Conversion (IMPRS-SurMat) for funding.

LG: investigation, data curation, conceptualization, investigation, formal analysis, visualization, writing—original draft; SPT: data curation, formal analysis, visualization, writing—review and editing; MR: investigation, writing—review and editing; RBV: investigation, writing—review and editing; PK: software, writing—review and editing; SZ: supervision, writing—review and editing; CS: supervision, writing—review and editing; BG: resources, supervision, conceptualization, writing—review and editing.

- [1] C. Y. Yap, C. K. Chua, Z. L. Dong, Z. H. Liu, D. Q. Zhang, L. E. Loh, and S. L. Sing, Review of selective laser melting: Materials and applications, *Appl. Phys. Rev.* **2**, 041101 (2015).
- [2] L. Dowling, J. Kennedy, S. O’Shaughnessy, and D. Trimble, A review of critical repeatability and reproducibility issues in powder bed fusion, *Mater. Des.* **186**, 108346 (2020).
- [3] P. Kontis, H. A. M. Yusof, S. Pedrazzini, M. Danaie, K. L. Moore, P. A. J. Bagot, M. P. Moody, C. R. M. Grovenor, and R. C. Reed, On the effect of boron on grain boundary character in a new polycrystalline superalloy, *Acta Mater.* **103**, 688 (2016).
- [4] E. J. Seo, L. Cho, Y. Estrin, and B. C. De Cooman, Microstructure-mechanical properties relationships for quenching and partitioning (Q&P) processed steel, *Acta Mater.* **113**, 124 (2016).
- [5] K. Biswas, J. He, I. D. Blum, C. I. Wu, T. P. Hogan, D. N. Seidman, V. P. Dravid, and M. G. Kanatzidis, High-performance bulk thermoelectrics with all-scale hierarchical architectures, *Nature (London)* **489**, 414 (2012).
- [6] D. L. Medlin and G. J. Snyder, Interfaces in bulk thermoelectric materials. A review for current opinion in colloid and interface science, *Curr. Opin. Colloid Interface Sci.* **14**, 226 (2009).
- [7] G. J. Snyder and E. S. Toberer, Complex thermoelectric materials, *Nat. Mater.* **7**, 105 (2008).
- [8] C. J. Vineis, A. Shakouri, A. Majumdar, and M. G. Kanatzidis, Nanostructured thermoelectrics: Big efficiency gains from small features, *Adv. Mater.* **22**, 3970 (2010).
- [9] W. Liu, H. S. Kim, Q. Jie, and Z. Ren, Importance of high power factor in thermoelectric materials for power generation application: A perspective, *Scr. Mater.* **111**, 3 (2016).
- [10] Y. Yu, C. Zhou, S. Zhang, M. Zhu, M. Wuttig, C. Scheu, D. Raabe, G. J. Snyder, B. Gault, and O. Cojocaru-Mirédin, Revealing nano-chemistry at lattice defects in thermoelectric materials using atom probe tomography, *Mater. Today* **32**, 260 (2020).
- [11] W. Kim and A. Majumdar, Phonon scattering cross section of polydispersed spherical nanoparticles, *J. Appl. Phys.* **99**, 084306 (2006).

- [12] S. Maier, S. Denis, S. Adam, J. C. Crivello, J. M. Joubert, and E. Alleno, Order-disorder transitions in the Fe₂VAI Heusler alloy, *Acta Mater.* **121**, 126 (2016).
- [13] D. D. D. Gu, W. Meiners, K. Wissenbach, and R. Poprawe, Laser additive manufacturing of metallic components: Materials, processes and mechanisms, *Int. Mater. Rev.* **57**, 133 (2012).
- [14] B. Song, X. Zhao, S. Li, C. Han, Q. Wei, S. Wen, J. Liu, and Y. Shi, Differences in microstructure and properties between selective laser melting and traditional manufacturing for fabrication of metal parts: A review, *Front. Mech. Eng.* **10**, 111 (2015).
- [15] M. Godec, S. Zaefferer, B. Podgornik, M. Šinko, and E. Tchernychova, Quantitative multiscale correlative microstructure analysis of additive manufacturing of stainless steel 316L processed by selective laser melting, *Mater. Charact.* **160**, 110074 (2020).
- [16] P. Bajaj, A. Hariharan, A. Kini, P. Kürnsteiner, D. Raabe, and E. A. Jäggle, Steels in additive manufacturing: A review of their microstructure and properties, *Mater. Sci. Eng. A* **772**, 138633 (2020).
- [17] J. H. Martin, B. D. Yahata, J. M. Hundley, J. A. Mayer, T. A. Schaedler, and T. M. Pollock, 3D printing of high-strength aluminium alloys, *Nature (London)* **549**, 365 (2017).
- [18] P. Kürnsteiner, M. B. Wilms, A. Weisheit, B. Gault, E. A. Jäggle, and D. Raabe, High-strength Damascus steel by additive manufacturing, *Nature (London)* **582**, 515 (2020).
- [19] J. Qiu, Y. Yan, T. Luo, K. Tang, L. Yao, J. Zhang, M. Zhang, X. Su, G. Tan, H. Xie, M. G. Kanatzidis, C. Uher, and X. Tang, 3D printing of highly textured bulk thermoelectric materials: Mechanically robust BiSbTe alloys with superior performance, *Energy Environ. Sci.* **12**, 3106 (2019).
- [20] H. Zhang, D. Hobbs, G. S. Nolas, and S. Leblanc, Laser additive manufacturing of powdered bismuth telluride, *J. Mater. Res.* **33**, 4031 (2018).
- [21] T. Kurzynowski, K. Gruber, W. Stopyra, B. Kuźnicka, and E. Chlebus, Correlation between process parameters, microstructure and properties of 316L stainless steel processed by selective laser melting, *Mater. Sci. Eng. A* **718**, 64 (2018).
- [22] L. Gomell, T. Haeger, M. Roscher, H. Bishara, R. Heiderhoff, T. Riedl, C. Scheu, and B. Gault, Microstructure manipulation by laser-surface remelting of a full-Heusler compound to enhance thermoelectric properties, *Acta Mater.* **223**, 117501 (2022).
- [23] L. Gomell, S. Katnagallu, A. D. Rassello, S. Maier, L. Perrière, C. Scheu, E. Alleno, and B. Gault, Chemical segregation and precipitation at anti-phase boundaries in thermoelectric Heusler-Fe₂VAI, *Scr. Mater.* **186**, 370 (2020).
- [24] L. Cordova, M. Campos, and T. Tinga, Revealing the effects of powder reuse for selective laser melting by powder characterization, *JOM* **71**, 1062 (2019).
- [25] M. Velasco-Castro, E. Hernández-Nava, I. A. Figueroa, I. Todd, and R. Goodall, The effect of oxygen pickup during selective laser melting on the microstructure and mechanical properties of Ti-6Al-4V lattices, *Heliyon* **5**, e02813 (2019).
- [26] J. D. Majumdar, Development of *in-situ* composite surface on mild steel by laser surface alloying with silicon and its remelting, *Surf. Coatings Technol.* **205**, 1820 (2010).
- [27] D. W. Wang, Y. H. Zhou, J. Shen, Y. Liu, D. F. Li, Q. Zhou, G. Sha, P. Xu, T. Ebel, and M. Yan, Selective laser melting under the reactive atmosphere: A convenient and efficient approach to fabricate ultrahigh strength commercially pure titanium without sacrificing ductility, *Mater. Sci. Eng. A* **762**, 138078 (2019).
- [28] L. Liu, C. Chen, R. Zhao, X. Wang, H. Tao, S. Shuai, J. Wang, H. Liao, and Z. Ren, *In-situ* nitrogen strengthening of selective laser melted Ti6Al4V with superior mechanical performance, *Addit. Manuf.* **46**, 102142 (2021).
- [29] A. I. P. Nwobu, R. D. Rawlings, and D. R. F. West, Nitride formation in titanium based substrates during laser surface melting in nitrogen-argon atmospheres, *Acta Mater.* **47**, 631 (1999).
- [30] M. Mikami, M. Inukai, H. Miyazaki, and Y. Nishino, Effect of off-stoichiometry on the thermoelectric properties of Heusler-type Fe₂VAI sintered alloys, *J. Electron. Mater.* **45**, 1284 (2016).
- [31] Y. Nishino, S. Kamizono, H. Miyazaki, and K. Kimura, Effects of off-stoichiometry and Ti doping on thermoelectric performance of Fe₂VAI Heusler compound, *AIP Adv.* **9**, 125003 (2019).
- [32] S.-P. Tsai, P. J. Konijnenberg, I. Gonzalez, S. Hartke, T. A. Griffiths, M. Herbig, K. Kawano-Miyata, A. Taniyama, N. Sano, and S. Zaefferer, Development of a new, fully automated system for EBSD-based large volume 3D microstructure mapping using serial sectioning by mechanical polishing, and its application to the analysis of special boundaries in 316L stainless steel, unpublished (2022).
- [33] P. J. Konijnenberg, S. Zaefferer, S. B. Lee, A. D. Rollett, G. S. Rohrer, and D. Raabe, Advanced methods and tools for reconstruction and analysis of grain boundaries from 3D-EBSD data sets, *Mater. Sci. Forum* **702–703**, 475 (2012).
- [34] K. Thompson, D. Lawrence, D. J. Larson, J. D. Olson, T. F. Kelly, and B. Gorman, *In situ* site-specific specimen preparation for atom probe tomography, *Ultramicroscopy* **107**, 131 (2007).
- [35] E. W. Lemmon and R. T. Jacobsen, Viscosity and thermal conductivity equations for nitrogen, oxygen, argon, and air, *Int. J. Thermophys.* **25**, 21 (2004).
- [36] See Supplemental Material at <http://link.aps.org/supplemental/10.1103/PhysRevMaterials.6.085405> for more background information, which includes Refs. [47–49].
- [37] M. Kamaya, Assessment of local deformation using EBSD: Quantification of local damage at grain boundaries, *Mater. Charact.* **66**, 56 (2012).
- [38] G. Bauer, V. Güther, H. Hess, A. Otto, O. Roidl, H. Roller, S. Sattelberger, S. Köther-Becker, and T. Beyer, Vanadium and vanadium compounds, in *Ullmann's Encyclopedia of Industrial Chemistry* (Wiley-VCH, Hoboken, 2016).
- [39] L. Gomell, M. Roscher, H. Bishara, E. A. Jäggle, C. Scheu, and B. Gault, Properties and influence of microstructure and crystal defects in Fe₂VAI modified by laser surface remelting, *Scr. Mater.* **193**, 153 (2021).
- [40] K. Y. Xie, A. J. Breen, L. Yao, M. P. Moody, B. Gault, J. M. Cairney, and S. P. Ringer, Overcoming challenges in the study of nitrided microalloyed steels using atom probe, *Ultramicroscopy* **112**, 32 (2012).
- [41] A. J. Breen, K. Y. Xie, M. P. Moody, B. Gault, H. W. Yen, C. C. Wong, J. M. Cairney, and S. P. Ringer, Resolving the morphology of niobium carbonitride nano-precipitates in steel using atom probe tomography, *Microsc. Microanal.* **20**, 1100 (2014).

- [42] H. Miyazaki, S. Tanaka, N. Ide, K. Soda, and Y. Nishino, Thermoelectric properties of Heusler-type off-stoichiometric $\text{Fe}_2\text{V}_{1+x}\text{Al}_{1-x}$ alloys, *Mater. Res. Express* **1**, 015901 (2014).
- [43] N. Mingo, D. Hauser, N. P. Kobayashi, M. Plissonnier, and A. Shakouri, “Nanoparticle-in-alloy” approach to efficient thermoelectrics: silicides in SiGe, *Nano Lett.* **9**, 711 (2009).
- [44] P. Carruthers, Scattering of phonons by elastic strain fields and the thermal resistance of dislocations, *Phys. Rev.* **114**, 995 (1959).
- [45] P. G. Klemens, Phonon scattering by Cottrell atmospheres surrounding dislocations, *J. Appl. Phys.* **39**, 5304 (1968).
- [46] L. Abdellaoui, Z. Chen, Y. Yu, T. Luo, R. Hanus, T. Schwarz, R. Bueno Villoro, O. Cojocar-Mirédin, G. J. Snyder, D. Raabe *et al.*, Parallel dislocation networks and Cottrell atmospheres reduce thermal conductivity of PbTe thermoelectrics, *Adv. Funct. Mater.* **31**, 2101214 (2021).
- [47] Z. Xiong, P. Zhang, C. Tan, D. Dong, W. Ma, and K. Yu, Selective laser melting and remelting of pure tungsten, *Adv. Eng. Mater.* **22**, 1901352 (2020).
- [48] H. Yamagata, W. Kasprzak, M. Aniolek, H. Kurita, and J. H. Sokolowski, The effect of average cooling rates on the microstructure of the Al-20% Si high pressure die casting alloy used for monolithic cylinder blocks, *J. Mater. Process. Technol.* **203**, 333 (2008).
- [49] J. Zhang, B. Song, Q. Wei, D. Bourell, and Y. Shi, A review of selective laser melting of aluminum alloys: Processing, microstructure, property and developing trends, *J. Mater. Sci. Technol.* **35**, 270 (2019).